

Assessing collection efficiency for a scintillator based high repetition radiography detector

Contact: jesel.patel@stfc.ac.uk

J. K. Patel

*Loughborough University,
LE11 3UE, United Kingdom.*

C. D. Armstrong, D. Neely

*Central Laser Facility, STFC,
OX11 0QX, United Kingdom.*

1 Introduction

Radiography is a technique which uses particle or high energy electromagnetic radiation to non-destructively probe optically impenetrable materials. Lasers have been demonstrated as novel sources for x-ray and particle radiography [1, 2]. Advancements in laser technology have enabled PetaWatt scale facilities at high repetition [3], allowing lasers to be the source for non-destructive imaging of a range of samples [4–6]. Operation at high repetition paves the way for techniques such as Computed Tomography [7] which demand 100s-1000s of acquisitions.

In order to use these new sources effectively, the detection system with which they are paired must also be able to operate at these high repetition rates. Traditional techniques typically use a passive detector plane such as image plate, or X-ray films which are currently limited in operable speed due to the nature of their readout. Scintillators paired with modern optical sensor technology (such as scientific cameras or silicon photomultipliers (SiPMs)) may provide a convenient solution for high repetition rate radiography, provided the particulars are properly considered.

To ensure a system is capable of the required sensitivity and dynamic range, the efficiency of conversion of energy deposited in the scintillator by incident radiation to detected optical photons needs to be understood. To that end, models for the collection efficiency are derived and discussed in the following report, in the context of available technology appropriate for use with a high power laser-plasma X-ray source.

2 Lens collection from a slab scintillator

To calculate the fraction of scintillation light produced in a slab scintillator which is collected by a lens of some diameter, $D = f/F$, where f is its focal length, and F is its F-number, we can calculate the solid angle it subtends at the scintillator, translated into the slab using Snell's law. We first assume that the scintillator slab is thin compared with the distance to the lens (i.e. the object distance $u = f(1+M)/M$, where M is the magnification of the system¹), and also that photons produced in the

scintillator are generated isotropically.

The half angle subtended by the lens at the scintillator is

$$\psi_2 = \tan^{-1} \left(\frac{D}{2u} \right), \quad (1)$$

$$= \tan^{-1} \left(\frac{M}{2F(1+M)} \right), \quad (2)$$

and the equivalent half angle inside the scintillator is

$$\psi_1 = \sin^{-1} \left(\frac{n_2}{n_1} \sin(\psi_2) \right), \quad (3)$$

$$= \sin^{-1} \left(\frac{n_2}{n_1} \sin \left(\tan^{-1} \left(\frac{M}{2F(1+M)} \right) \right) \right), \quad (4)$$

where n_1 is the refractive index of the imaging immersion medium (usually air, where $n_1 \approx 1$), and n_2 is the refractive index of the scintillator.

If we consider an X-ray depositing energy in a scintillator at the point in the centre of the camera's field of view, figure 1. shows that from this half angle, ψ_1 , we can calculate the fraction of an isotopic scintillation emission which will subsequently be collected by the lens. The fraction of collected photons to scintillation photons is given by the fractional solid angle of the cone with half angle ψ_1 , multiplied by a factor of $(1 + R_{entr.})$ to account for a rear cone which is reflected by the entrance surface of the scintillator due to a coating with reflectivity, $R_{entr.}$. This cone will internally reflect in the scintillator, but then can exit through the imaged surface and be collected by the lens, exiting at the same angle, ψ_2 . The fractional solid angle is given by

$$\frac{\Omega}{4\pi} = \frac{2\pi(1 - \cos(\psi_1))}{4\pi} = \frac{1 - \cos(\psi_1)}{2} \quad (5)$$

The collected fraction is therefore given by the equation

$$\frac{N_{coll.}}{N_{scint.}} = \frac{(1 + R_{entr.})}{2} (1 - \cos(\psi_1)). \quad (6)$$

Substituting equation (4) into equation (6) leads to our complete model for lens coupled collection efficiency. However, as can be seen as it is presented in equation (7), this is rather unwieldy in form. In low magnification ($M < 1$) this equation simplifies due to paraxial

¹here we define M as the ratio of the scintillator image lateral size on the detector to the 'object' scintillator lateral size

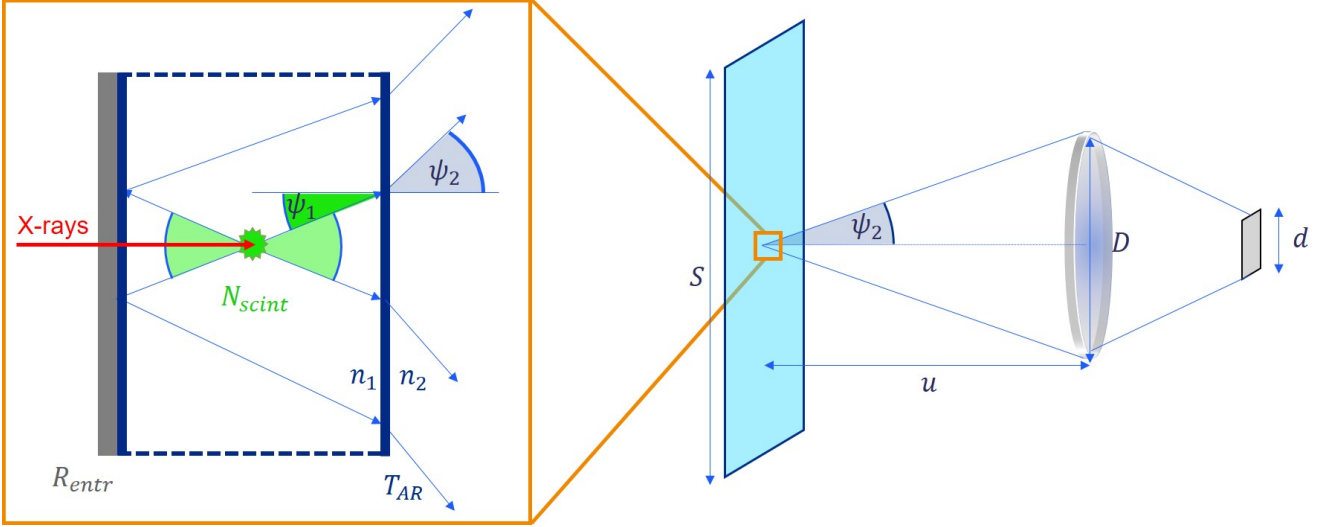


Figure 1: Scintillator imaging diagram on the right-hand side illustrating geometry of lens collection, and blown up cross section of modelled isotropic scintillation event, with relevant angles for calculating lens collection efficiency based on Snell's law and solid angles. Reflected rear cone and refractive indices of the scintillator and air (or alternate immersion medium) are also shown.

$$\frac{N_{coll.}}{N_{scint.}} = \frac{(1 + R_{entr.})}{2} \left(1 - \cos \left(\sin^{-1} \left(\frac{n_2}{n_1} \sin \left(\tan^{-1} \left(\frac{M}{2F(1+M)} \right) \right) \right) \right) \right) \quad (7)$$

approximations, i.e.

$$\left. \begin{aligned} \sin \theta, \sin^{-1} \theta &\approx \theta \\ \tan \theta, \tan^{-1} \theta &\approx \theta \\ \cos \theta &\approx 1 - \frac{\theta^2}{2} \end{aligned} \right\} \text{ when } M < 1.$$

Using the above approximations, equation (7) reduces to

$$\frac{N_{coll.}}{N_{scint.}} = \frac{n_2^2(1 + R_{entr.})}{4n_1^2} \frac{1}{4F^2} \frac{M^2}{(1 + M)^2}, \quad (8)$$

where the first factor is the fraction of photons which exit the scintillator,

$$\frac{N_{exit}}{N_{scint.}} = \frac{n_2^2(1 + R_{entr.})}{4n_1^2}, \quad (9)$$

and the subsequent factors are the fraction of exiting photons which are collected by the lens,

$$\frac{N_{coll.}}{N_{exit}} = \frac{1}{4F^2} \frac{M^2}{(1 + M)^2}. \quad (10)$$

The difference in the performance of the two models in eqs. (7) and (8) for real machine vision prime lenses and Mitutoyo objectives is shown in fig. 2 to demonstrate the failure of the paraxial approximation of the model approaching high magnification ($M > 5$).

Finally, we can also include the transmission of the front face of the scintillator, assuming it is anti-reflective

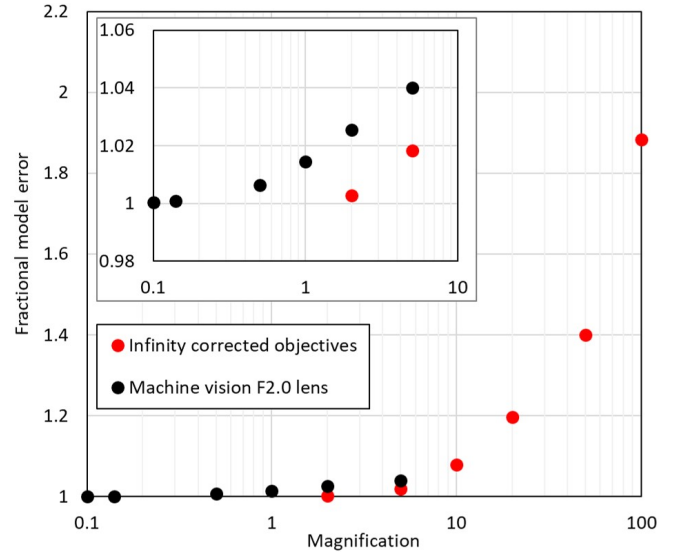


Figure 2: Error of the paraxially approximated lens collection model, as a fraction of the more complete model. Inset is scaled up to show small errors at $M < 1$. The F and effective magnification with a machine vision lens [8] and Mitutoyo infinity corrected, long working distance objectives [9] were used to simulate real operating conditions in low and high magnification, respectively. The insert shows the $0.1 < M < 10$ region with a magnified y-scale.

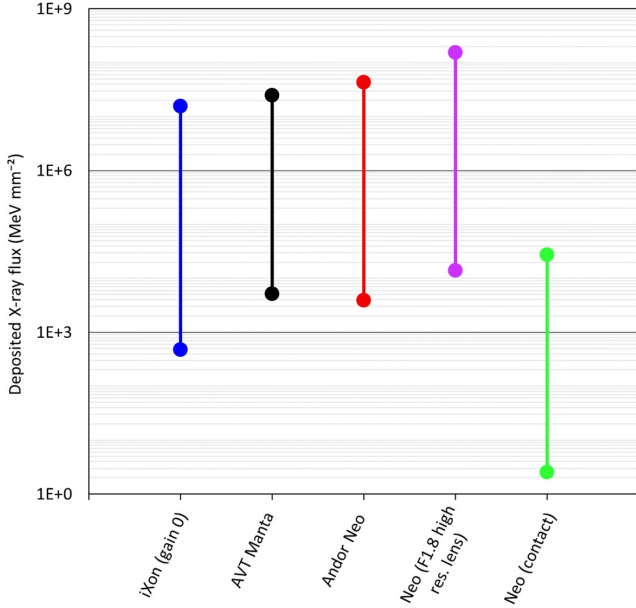


Figure 3: Example application of the low magnification scintillator imaging model, demonstrating the dynamic range of a LYSO radiography instrument using various cameras and lens or contact optical couplings. Given in deposited energy per scintillator area, the model can be used to predict whether different imaging systems are appropriate with a source of a given flux and spectral shape. The examples are an EMCCD Andor iXon 13.3×13.3 mm sensor, an AVT Manta CMOS Gig-E camera, and a scientific CMOS Andor Neo, all coupled with F0.95 Navitar lenses. In addition the Andor Neo sensor is shown coupled with a high resolution F1.8 lens, and as a theoretically contact coupled Neo sensor over an entire 100×100 mm² scintillator. The dynamic range of the camera sensors was calculated from measurements in Reference [10].

(AR) coated, T_{AR} , and to find the fraction of photons which are detected by the optical sensor, we should include the lens transmission, T_{lens} and the quantum efficiency of the chip, Q_E . Note that T_{lens} and Q_E are functions of the scintillator emission wavelength, λ_γ , but we will omit the function notations for brevity:

$$\frac{N_{det.}}{N_{scint.}} = \frac{n_2^2 T_{AR} (1 + R_{entr.})}{4n_1^2} \frac{1}{4F^2} \frac{Q_E M^2}{(1 + M)^2}. \quad (11)$$

In fig. 3 the model in eq. (11) is used to demonstrate the relative performance of different optical couplings with a 100×100 mm² LYSO slab ($n_1 = 1.8$), with an aluminium reflective rear coating of $R_{entr.} = 0.7$, assumed perfect transmission through an anti-reflective coating ($T_{AR} = 1$).

To obtain the expected number of photons detected by the system we need to multiply through by the number of photons produced in the scintillator. The two components of this process are the deposition of X-ray

energy into electrons in the scintillator, and the conversion of these excited electrons into optical photons.

Ignoring secondary scattering effects, the deposited X-ray energy is given by Beer's law,

$$E_{dep.} = E_X (1 - e^{-\mu_m \rho \tau}), \quad (12)$$

where E_X is the energy of an incident X-ray photon, μ_m is the mass attenuation coefficient of the scintillator material [$\text{cm}^2 \text{g}^{-1}$], ρ is the mass density [g cm^{-3}] and τ is the path length of the X-ray in the scintillator (i.e. the scintillator thickness). While the physics of electron transport to luminescent centres and subsequent radiative decay are an active research area, scintillators are generally characterised empirically by an efficiency factor, κ - the number of optical photons produced per MeV of deposited radiation energy [photons MeV^{-1}]. So $N_{scint.} = E_{dep.} \kappa$, and the number of detected photons is

$$N_{det.} = E_{dep.} \kappa \frac{n_2^2 T_{AR} (1 + R_{entr.})}{4n_1^2} \frac{1}{4F^2} \frac{Q_E M^2}{(1 + M)^2}. \quad (13)$$

2.1 Resolution element in a slab scintillator

Assuming that scintillation light is on average emitted at a depth $\tau/2$ into the scintillator, a resolution element based on optical spreading can be defined as

$$\Delta S_{opt.} = \sqrt{\left(\frac{D\tau n_2}{2un_1}\right)^2 + \left(R_{entr.} \frac{3D\tau n_2}{2un_1}\right)^2} \quad (14)$$

$$= \sqrt{\left(\frac{D\tau n_2}{2un_1}\right)^2 (1 + 3R_{entr.})^2}. \quad (15)$$

There is also a significant reduction in resolution due to lateral spreading of excited electrons when high energy X-rays are incident. Monte Carlo GEANT simulations have been performed to determine the extent of this spreading, such that a complete definition of a resolution element of a slab scintillator can be written as

$$\Delta S = \Delta S_{opt.} + \Delta S_e, \quad (16)$$

where ΔS_e is the contribution of the electron spreading.

3 Pixelated scintillators

In contrast to a simple slab scintillator, the photons generated in a pixelated scintillator with a diffuse reflective coating such as PTFE will have a higher probability of exiting, depending on the reflectivity of the coating, and geometry of the pixel. A scintillator pixel can be modelled as a spherical cavity with a transmissive exit face. The details of such modelling are given in Reference [11], where an assumption that scintillation is homogenous allows a simplification which gives that the fraction of scintillation photons which exit a pixel is

$$\frac{N_{exit}}{N_{scint.}} = \frac{X'}{1 - R + RX'}, \quad (17)$$

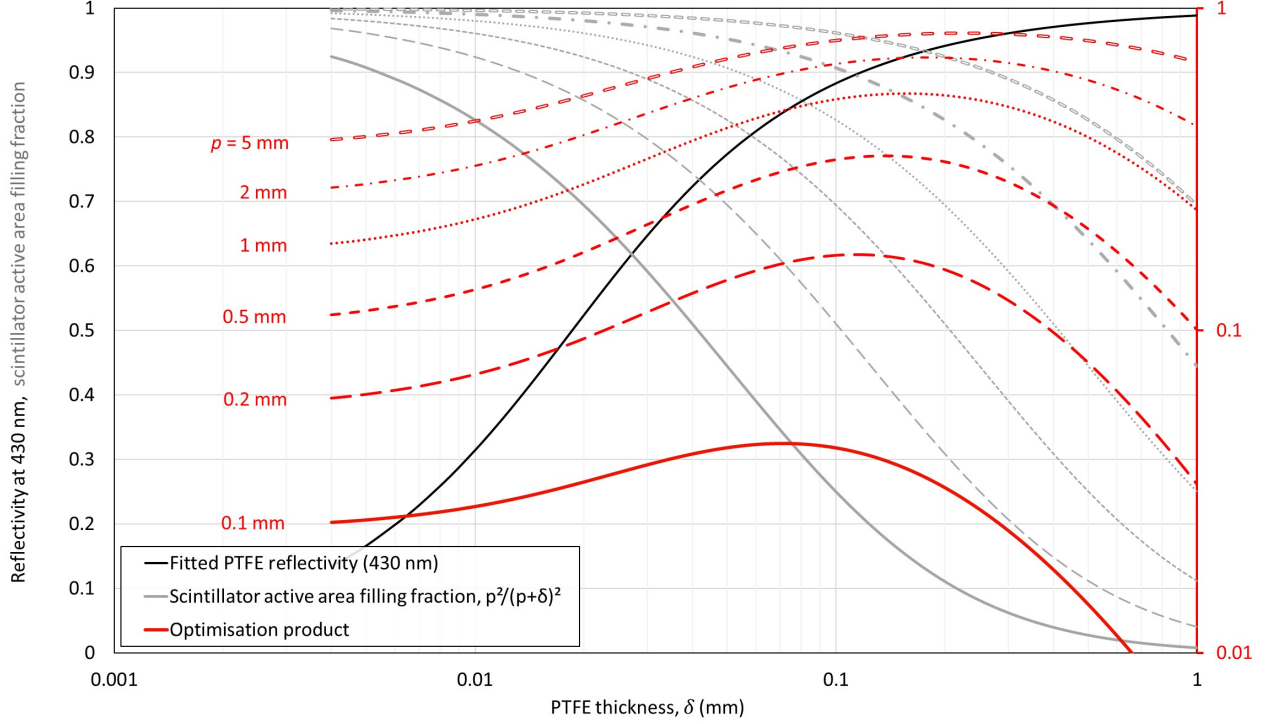


Figure 4: Optimisation curves (red) for the thickness of reflective PTFE coating with various pixel sizes, based on the reflectivity of PTFE (black) and the scintillator active area filling fraction (grey).

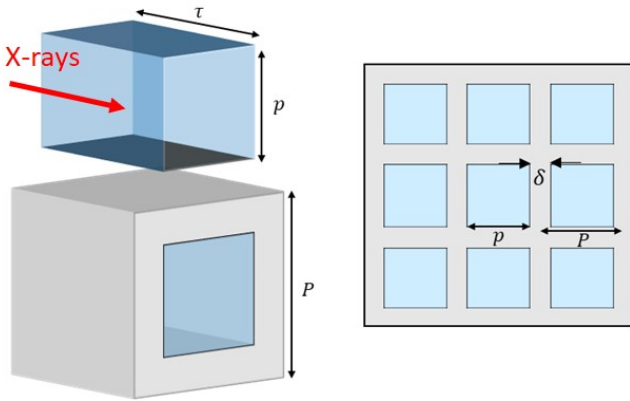


Figure 5: Reflectively wrapped scintillator pixel geometry and dimensions, with a 2D illustration of a small section of a pixelated scintillator array. p is the active scintillator lateral size, δ is the thickness of reflective coating, and P is the pixel pitch.

where X' is related to the geometry of the pixel, the area of the exit face, and the refractive indices of the scintillator (n_1) and coupled medium (n_2) such that

$$X' = \frac{p^2 \frac{n_2^2}{2n_1^2}}{p^2 \left(1 + \frac{n_2^2}{2n_1^2}\right) + 4p\tau} \quad (18)$$

$$= \frac{\frac{n_2^2}{2n_1^2}}{\left(1 + \frac{n_2^2}{2n_1^2}\right) + 4\tau/p}, \quad (19)$$

where τ is the scintillator depth as per previously, and p is the active pixel lateral size, illustrated in figure 5. (top-left).

In order to compare a pixelated scintillator to a slab, we will use the models to consider their performance with the same flux of some energy distribution of X-rays. The deposition and conversion efficiency per X-ray is the same in each case, but the equivalent converted X-ray flux is necessarily smaller in a pixelated array. This is due to the active area filling fraction of an array

$$\frac{p^2}{P^2} = \frac{p^2}{(p + \delta)^2} \quad (20)$$

where P is the total pixel pitch, and δ is the reflective material (e.g. PTFE) filled pixel separation (see figure 5.). This factor determines the fraction of X-ray flux which is incident to active scintillator material. Better

X-ray conversion is achieved by reducing the thickness of the reflective coating, δ , however, the reflectivity of the coating is also related to its thickness, resulting in reduced optical output per pixel. Fitting to data from Reference [12] with a \tan^{-1} function gives

$$R_{pixel} \approx \frac{2}{\pi} \tan^{-1}(53.8\delta) \quad (21)$$

for PTFE, and plotting the product of equations (20) and (21) as a function of δ allows the identification of the pixel separation for a given active area which is optimal with respect to the trade-off between reflectivity and X-ray collection. Figure 4. shows how the optimal thickness, δ , reduces with smaller pixel size, to minimise X-ray collection loss. This consideration gives that the effective number of scintillation photons produced by the scintillator array per X-ray flux is reduced by the filling factor, so that the total optical yield per pixel is

$$N_{exit} = \Phi_X \frac{p^2}{P^2} \cdot E_{dep.} \kappa \frac{X'}{1 - R + RX'}, \quad (22)$$

where Φ_X is the X-ray flux through the pixel pitch area, P^2 .

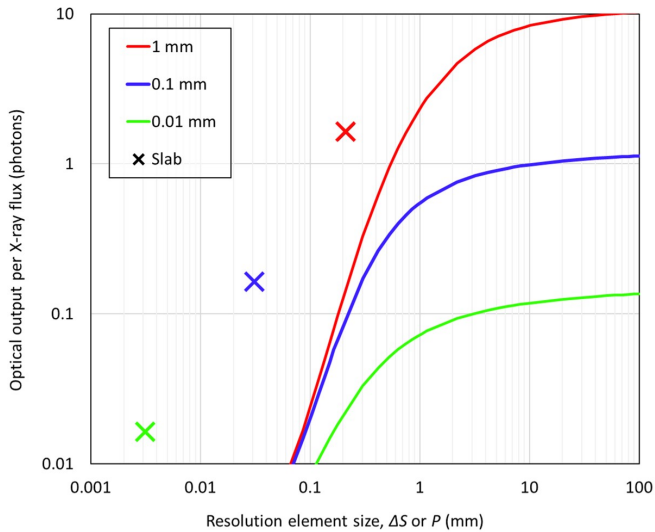


Figure 6: Modelled optical output from slab (crosses) and pixelated (lines) LYSO scintillators per unit flux of 1 MeV X-rays, for three thicknesses, plotted against the size of the smallest resolution element, ΔS or P . The resolution of the slabs, were calculated based on the effective optical spreading in a low optical magnification ($M = 1/7$) configuration, with a $f = 50$ mm, F0.95 lens, and Monte Carlo GEANT simulations of lateral electron spreading. The output and pitch size of the pixelated arrays were calculated with optimised PTFE reflective coating thicknesses for varied lateral pixel sizes.

Now we can compare the optical outputs from a pixelated array and a slab when under the same conditions. For example, figure 6. shows the number of scintillation

photons which exit slab and pixel LYSO scintillators at three thicknesses ($\tau = 1, 0.1, 0.01$ mm) per unit flux of 1 MeV X-rays. For the pixelated scintillators, the output is shown as a function of the pixel pitch, P , as the smallest resolution element, while the slab outputs are plotted against ΔS , as calculated from eq. (16), using aforementioned simulations to determine ΔS_e , and some typical values for a low-magnification optical configuration to calculate $\Delta S_{opt.}$ (an $f = 50$ mm, F0.95 lens, with $M = 1/7$, and an aluminium mirrored rear surface, $R_{entr.} = 0.7$). Evidently, pixelated scintillators can offer higher optical output, but only at the cost of significantly worse resolution. Pixelated arrays might therefore find more use in configurations with the object near a point X-ray source such that it is highly magnified at the scintillator plane.

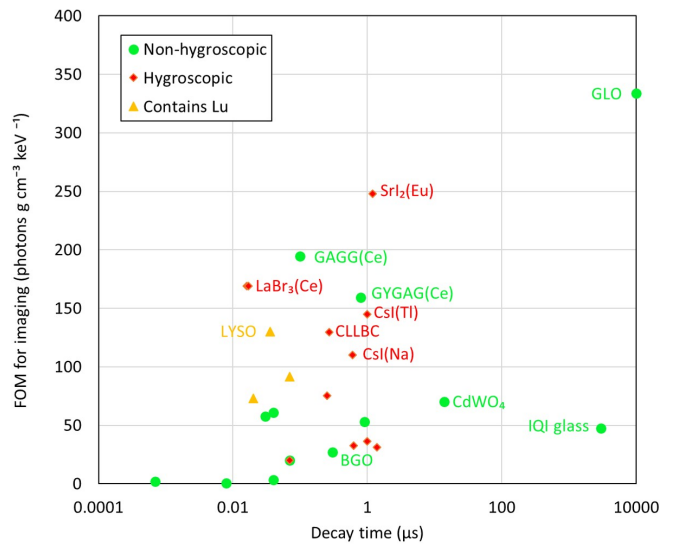


Figure 7: Figures of merit for surveyed inorganic X-ray scintillators, plotted against their primary scintillation decay times. Scintillators with decay times $> 100 \mu s$ are unsuitable for operation at kHz repetition rates. Hygroscopic scintillators (red diamonds) require hermetic sealing to prevent clouding over extended use, and scintillators containing Lutetium (yellow triangles) will present a self-activated background glow in large volumes due to the presence of a naturally occurring radioisotope.

4 Figure of merit

To compare scintillator candidates for a radiography detector, we describe a scintillator figure of merit as

$$\varepsilon = \frac{\rho \kappa}{n_1}. \quad (23)$$

This encapsulates the key aspects of relevant scintillator behaviour. Energy deposition is dependant on the areal density,

$$E_{dep.} \propto \rho \tau, \quad (24)$$

which is shown by the Taylor expansion of eq. (12), assuming a thin scintillator (< 1 mm) and sufficiently energetic X-rays (> 100 keV). The photon generation is therefore a combination of $\rho\tau\kappa$, and for a fixed length and lens system, the photon collection is dependant only on the refractive index, n_1 , leaving the figure of merit in eq. (23).

Fig. 7 shows the figures of merit for various inorganic X-ray scintillators, and highlights some potential candidates for a radiography detector. GLO has an excellent figure of merit, but has a decay time unsuitable for high repetition operation. GAGG(Ce) and GYGAG(Ce) are good potential future candidates, although new considerations with respect to long-lifetime afterglows indicate that GAGG(Ce) is likely to also be unsuitable without further development, and GYGAG(Ce) is currently highly expensive to obtain commercially. LYSO is the next best chemically rugged option, despite a low level self activation which shouldn't pose too much of an issue for thin slabs. If the scintillators can be appropriately hermetically sealed, $\text{LaBr}_3(\text{Ce})$, CeBr_3 and $\text{CsI}(\text{Tl})$ may be good options, while $\text{SrI}_2(\text{Eu})$ is currently costly and not manufactured in the likely required sizes.

5 Conclusion

Models for the collection efficiency of scintillator based radiography detector systems have been presented to predict design suitability for use with a high power laser X-ray source. The error of a paraxially approximated model are negligible ($< 2\%$) for lens coupled systems at low optical magnification ($M < 1$), while a more complex model can be used for predicting collection in a high magnification environment. Use of pixelated scintillators is demonstrated to only increase optical output at the detriment of resolution, although this may be redeemed by placing objects close to a point source for increased geometrical magnification at the scintillator plane.

An approximate figure of merit has been used to suggest potential candidates for low magnification detectors, however, further work is required to address the long lifetime afterglow components observed in many scintillators, in order to more accurately select one which is appropriate for operation at high repetition.

6 Appendix - increased vignetting in lens coupled system

The previous modelling for the lens collection of scintillator photons assume X-ray energy is deposited in a small region at the centre of a scintillator. However, elements at the edges of a scintillator surface, or array, will subtend a smaller solid angle at the camera lens, and similarly, the lens will subtend a smaller solid angle of the emitted flux from off-axis elements. This gives rise to a $\cos^4\theta$, where θ is the angle of the lens to normal at the scintillator element, which causes significant

a vignetting effect in the image, with reduction in signal even for small angles $\sim 30\%$.

For long object distances in low magnification operation ($u \ll D$), the solid angle subtended by the lens at an element on the scintillator surface is given by

$$\Omega_{lens} \approx \frac{A}{u'^2}, \quad (25)$$

where A is the area of the lens aperture, and u' is the radius of a spherical surface subtended at an area element on the scintillator surface or array.

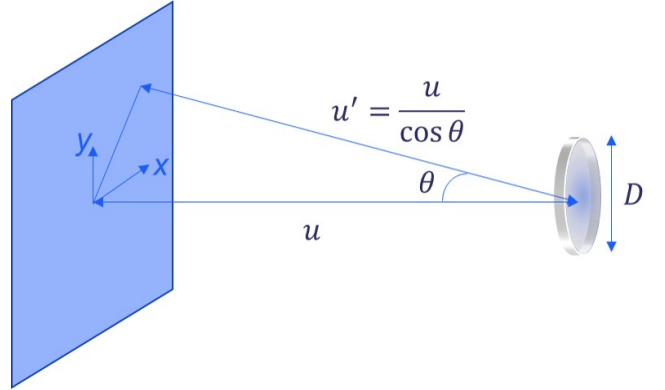


Figure 8: Illustration of the increased distance between a lens and elements on a scintillator surface which are off-centre, resulting in a reduced effective solid angle subtended by the lens, and subsequently reduced collected optical flux.

Viewing the lens at some angle, θ , to the surface normal, it appears as an ellipse with an area

$$A = \frac{\pi D}{2} a, \quad (26)$$

where a is the minor axis of the ellipse. Assuming θ is small (< 1 rads), $a \approx \frac{\pi D}{2} \cos\theta$, so

$$A(\theta) = \frac{\pi D^2}{4} \cos\theta. \quad (27)$$

For an element on the surface with an angular displacement $\theta = \arctan\left(\frac{\sqrt{x^2+y^2}}{u}\right)$,

$$u' = \frac{u}{\cos\theta}. \quad (28)$$

Substituting $A(\theta)$ and u' into eq. (25),

$$\Omega_{lens}(\theta) = \frac{\pi D^2}{4u^2} \cos^3\theta. \quad (29)$$

Previous work has demonstrated that scintillators behave as approximate Lambertian emitters [13]. A Lambertian emission is characterised by a number of photons per steradian which decreases as $\cos\theta$, so the

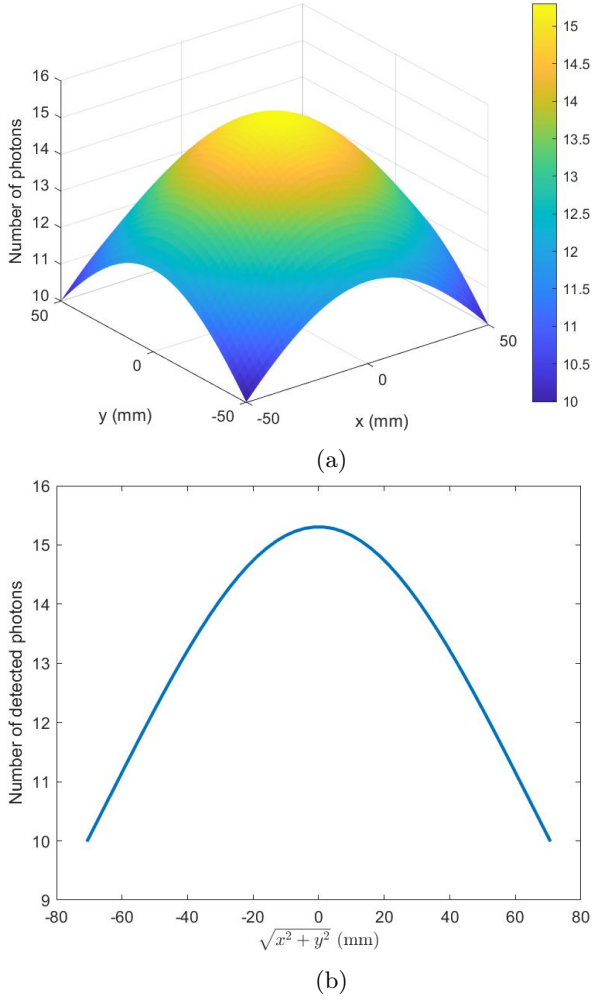


Figure 9: Photon detection non-uniformity across the image of a 100×100 mm slab LYSO scintillator, for 1 MeV X-ray deposition in each imaged area element.

combined effect is a vignette $\propto \cos^4 \theta$. Thus the complete model for the total detected number of photons from a slab becomes

$$N_{det.} = E_X (1 - e^{-\mu_m \rho \tau}) \cdot \frac{\kappa T_{AR} (1 - R_{entr.}) n_2^2}{4n_1^2} \cdot \frac{T_{lens}}{4F^2} \frac{Q_E M^2}{(1 + M)^2} \cos^4 \theta, \quad (30)$$

and for a pixelated scintillator,

$$N_{det.} = E_X (1 - e^{-\mu_m \rho \tau}) \cdot \frac{\kappa X'}{1 - R + RX'} \cdot \frac{T_{lens}}{4F^2} \frac{Q_E M^2}{(1 + M)^2} \cos^4 \theta. \quad (31)$$

References

- [1] C. D. Armstrong, PhD Thesis, 2019 *Bremsstrahlung radiation and fast electron transport in laser-plasma interactions* University of Strathclyde, Glasgow
- [2] C. Brenner, S. R. Mirfayzi, D. R. Rusby et al., 2015 *Laser-driven x-ray and neutron source development for industrial applications of plasma accelerators* Plasma Physics and Controlled Fusion, Volume 58, Number 1, <https://doi.org/10.1088/0741-3335/58/1/014039>
- [3] H. Towrie, *The Science and Technology Behind EPAC*, <https://www.clf.stfc.ac.uk/Pages/EPACs-Science.aspx>
- [4] D. Haden, S. Chen, B. Zhao, et al., 2016, *High-resolution radiography of thick steel objects using an all-laser-driven MeV-energy X-ray source* Proc. SPIE 9964, Advances in Laboratory-based X-Ray Sources, Optics, and Applications V, 99640G, <https://doi.org/10.1117/12.2241606>
- [5] C. P. Jones, C. M. Brenner, C. A. Stitt, et al., 2016, *Evaluating laser-driven Bremsstrahlung radiation sources for imaging and analysis of nuclear waste packages*. Journal of hazardous materials. pp. 694-701. ISSN 0304-3894 <https://doi.org/10.1016/j.jhazmat.2016.07.057>
- [6] J. M. Cole, D. R. Symes, N. C. Lopes, et al., 2016 *High resolution imaging of embryonic mouse samples with a laser-driven betatron x-ray source* CLF Annual Report, STFC, Rutherford Appleton Laboratory. <https://doi.org/10.1073/pnas.1802314115>
- [7] J. M. Cole, D. R. Symes, N. C. Lopes, et al., 2018 *High-resolution μ CT of a mouse embryo using a compact laser-driven X-ray betatron source* PNAS, 115 (25) 6335-6340, <https://doi.org/10.1073/pnas.1802314115>
- [8] Thorlabs, Inc., 2020 <https://www.thorlabs.com/thorproduct.cfm?partnumber=MVL25M43>
- [9] Edmund Optics, Ltd., 2020 <https://www.edmundoptics.co.uk/f/mitutoyo-infinity-corrected-long-working-distance-objectives/12298/>
- [10] A. Dasgupta, C. D. Armstrong, D. Neely, D. R. Rusby, G. G. Scott *Assessment of cameras for low intensity acquisitions* CLF Annual Reports, 2018, STFC, Rutherford Appleton Laboratory.
- [11] J. K. Patel, C. D. Armstrong, D. Neely et al., 2020, *Compact scintillator - silicon photomultiplier hard X-ray detectors for laser-plasma diagnosis* CLF Annual Report, STFC, Rutherford Appleton Laboratory.
- [12] M. Janecek, 2012 *Reflectivity Spectra for Commonly Used Reflectors* IEEE Transactions on Nuclear Science **59**, **3**, 490-497. DOI: 10.1109/TNS.2012.2183385
- [13] J. K. Patel, C. D. Armstrong, D. Neely, R. J. Clarke, 2020, *Angular emission of optical flux from scintillator crystals* CLF Annual Reports, STFC, Rutherford Appleton Laboratory.